OPTICA QUANTUM

CMOS photonic integrated source of broadband polarization-entangled photons

Alexander Miloshevsky, [1,*] Lucas M. Cohen, [2,†] Karthik V. Myilswamy, [2,†] Muneer Alshowkan, [1] Saleha Fatema, [2] Hsuan-Hao Lu, [1] Andrew M. Weiner, [2] AND Joseph M. Lukens [1,3]

[1] Quantum Information Science Section, Computational Sciences and Engineering Division, Oak Ridge National Laboratory, Oak Ridge, Tennessee 37831, USA
[2] School of Electrical and Computer Engineering and Purdue Quantum Science and Engineering Institute, Purdue University, West Lafayette, Indiana 47907, USA
[3] Research Technology Office and Quantum Collaborative, Arizona State University, Tempe, Arizona 85287, USA
[†] These authors contributed equally to this work.
*miloshevskya@ornl.gov

Received 15 February 2024; revised 10 June 2024; accepted 1 July 2024; published 12 August 2024

We showcase a fully on-chip CMOS-fabricated silicon photonic integrated circuit employing a bidirectionally pumped microring and polarization splitter-rotators tailored for the generation of broadband (>9 THz), high-fidelity (90–98%) polarization-entangled photons. Spanning the optical C+L-band and producing over 116 frequency-bin pairs on a 38.4-GHz-spaced grid, this source is ideal for flex-grid wavelength-multiplexed entanglement distribution in multiuser networks.

https://doi.org/10.1364/OPTICAQ.521418

Quantum networks of the future [1] must be flexible to distribute entanglement on demand to multiple end-users, adapt to user resource requirements, and maneuver unexpected disruptions to communication channels. To this end, recent experiments combining broadband polarization entanglement with wavelength-selective switches (WSSs) chart a promising path forward [2–4]. Leveraging concepts proven in classical "flex-grid" or "elastic" optical networking [5], the center wavelength, bandwidth, and lightpath of any quantum demand can be reconfigured adaptively. In this paradigm, broadband and compact polarization-entangled sources—ideally via scalable, CMOS integrated photonics—are of critical importance. Multiple approaches for the on-chip generation of polarization-entangled photons have been proposed and demonstrated; examples employing spontaneous four-wave mixing (SFWM) in silicon include polarization rotation in a single waveguide [6], parallel waveguides combined with a two-dimensional grating coupler [7], and multi-spatial-mode interactions [8], while type-II parametric downconversion in AlGaAs has also proven extremely successful [9].

Ubiquitous in silicon photonics, microring resonators (MRRs) enable resonantly enhanced SFWM for pair generation with higher brightness (flux per unit bandwidth) than single-pass waveguide structures, all with a more compact footprint [10]. While producing frequency-bin entanglement automatically [11,12], the direct generation of polarization entanglement in MRRs is complicated by the distinct spatial profiles and effective indices for orthogonally polarized modes, leading to mismatched spectral resonances for transverse electric (TE) and transverse magnetic (TM) fields and preventing the direct generation of polarization entanglement. Although spectral matching can in principle be realized via separate MRRs coupled to the same waveguide (one aligned for TE and the other for TM), such an approach demands tight fabrication tolerances for broadband operation [13]. This situation has motivated designs in which an MRR is placed in a fiber Sagnac loop to convert copolarized but counterpropagating amplitudes into a polarization-entangled output [14,15]—a solution that unfortunately sacrifices compactness for functionality. Accordingly, integrated sources of polarization entanglement have so far been limited either by: (i) adopting a nonresonant on-chip solution with lower efficiency; (ii) integrating distinct MRRs that must be spectrally aligned with tight control; or (iii) enlisting a single efficient MRR but supplementing it with off-chip fiber-optic manipulation to synthesize polarization entanglement.

Here we propose a novel solution combining bidirectional pumping with integrated polarization splitter-rotators (PSRs) for a complete on-chip, MRR-based, CMOS-fabricated polarization-entangled source. We verify high-fidelity operation through quantum state tomography (QST) of 116 individual channel pairs and various channel groupings across the full optical C+L-band, confirming the viability of flexible bandwidth allocations as well as the trade-off between fidelity and flux due to multipair emission and polarization-mode dispersion (PMD).

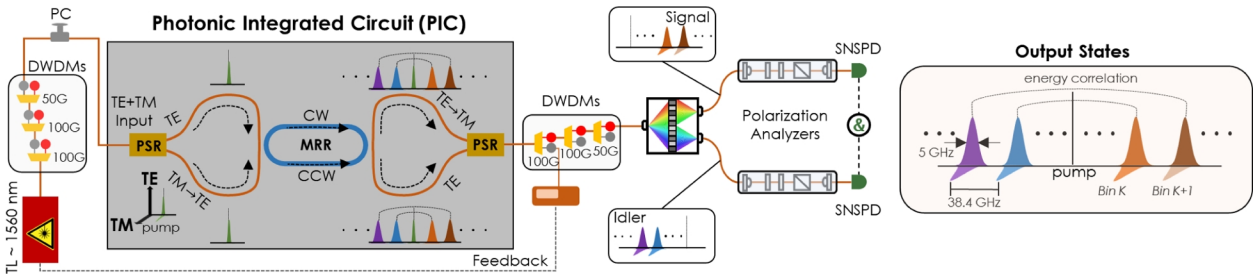

Fig. 1. Experimental setup including conceptual diagrams of the polarization-frequency states at various stages. TL, continuous-wave tunable laser; DWDM, dense wavelength-division multiplexer; PC, polarization controller; TE, transverse electric; TM, transverse magnetic; PSR, polarization splitter-rotator; MRR, microring resonator; SNSPD, superconducting nanowire single-photon detector.

Figure 1 illustrates the experimental setup for generating and characterizing the wavelength-multiplexed polarization-entangled state. We use a continuous-wave laser (Santec TSL-570) to pump the chip and set the central wavelength to the ring resonance at ~1559.85 nm. To attenuate background noise in the pump laser, we incorporate three dense wavelength-division multiplexers (DWDMs): two with a 100-GHz passband and one with a 50-GHz passband, all centered around 1559.81 nm. Following the DWDMs, a polarization controller (PC) manages the ratio of TE and TM polarization coupled into the chip (~8 dBm estimated on-chip power).

Designed for and manufactured by the AIM Photonics multi-project wafer service [16], our device leverages polarization-independent spot-size converters to couple light of both polarizations onto the chip. The PSR spatially separates the TE and TM inputs, rotating the TM portion to TE. A variety of approaches have been exploited for PSRs in silicon photonics, often using an anisotropic waveguide design to hybridize the polarization modes, for example, using different upper and lower cladding materials or by implementing a partial etch in the waveguide [17]. The physical design of our specific PSR is proprietary, but has been shown to realize ~0.65 dB (<0.3 dB) insertion (polarization-dependent) loss [18], and we have independently measured an extinction ratio of ~30 dB (~15 dB) between the two outputs for a TE (TM) input state.

After the first PSR, the pump photons bidirectionally couple into a racetrack-shaped MRR with 500-nm-wide by 220-nm-thick silicon single-mode waveguides throughout and adiabatic curves and directional couplers in the coupling sections [19]. The MRR was designed for a free spectral range of 38.4 GHz and intrinsic (loaded) Q factor of 3.7 $\times 10^5$ (3.7×10^4) under the assumption of 2 dB cm^{-1} waveguide loss; experimentally we measured a loaded Q factor of $\sim 3.4 \times 10^4$ near the pump resonance. Resistive microheaters are embedded within the MRR, and in each output path for frequency and phase tuning, but are not employed here.

After extracting the TE-polarized frequency-bin-entangled photons generated via SFWM in both directions of the MRR, a second PSR reverts one pathway to TM polarization before recombining with the unrotated TE pathway. Ideally, the output is an equal coherent superposition of two counterpropagating SFWM processes, where signal and idler photons form a biphoton frequency comb with a frequency spacing (38.4 GHz) and linewidth (~5-GHz FWHM) defined by the MRR. Each pair of energy-matched resonances manifests a polarization Bell state $|\Phi^+\rangle = \frac{1}{\sqrt{2}}(|H_{\omega_k} H_{\omega_{-k}}\rangle + |V_{\omega_k} V_{\omega_{-k}}\rangle)$, where TE (TM) is identified with horizontal H (vertical V) polarization and the integer $k \geq 1$ denotes the k^{th} frequency-bin pair (number of resonances away from the pump).

Upon exiting the chip, another set of three DWDMs, replicating the prior configuration, isolates the newly generated broadband entangled photons from the residual pump light, with an estimated pump suppression of ~68 dB and net reflection loss of 3 dB for the entangled photons. Additionally, we implement a feedback loop that monitors the optical power in the pass channel of the first output DWDM, ensuring the pump aligns with the intended cavity resonance in the presence of real-time thermal drift. Finally, we employ a Fourier-transform pulse shaper (Finisar Waveshaper 4000B; 6.5-dB loss) as a WSS to route two frequency bins, one from the signal side of the spectrum and one from the idler, to two separate optical fibers for subsequent state characterization. Two-qubit polarization QST is carried out using a pair of motorized polarization analyzers (each consisting of two collimators, a quarter-wave plate, a half-wave plate, and a polarizing beam splitter cube, for a total throughput of ~70%) followed by photon detection with superconducting nanowire single-photon detectors (Quantum Opus; >81% efficiency) connected to a photon-counting module (PicoQuant TimeHarp).

As an aside, we note that the first PSR in Fig. 1 is not strictly necessary but could be replaced by a Y-branch, so that all fields of interest would be TE-polarized until the final PSR combiner. In practice, however, the need to adjust the pump power in each path (clockwise and counterclockwise) to counteract any imbalances in loss or efficiency would necessitate a tunable beam splitter—requiring, e.g., a Mach–Zehnder interferometer (MZI)—in lieu of a fixed Y-branch. Thus, our choice of the first PSR is inspired by convenience, as it permits *passive* control of the splitting ratio via the input laser polarization, rather than active electrical control in an MZI.

We first characterize the MRR by measuring the joint-spectral intensity (JSI) under unidirectional pumping. We tune the PC to excite only the TE or TM polarization, bypass both polarization analyzers, and program the pulse shaper to scan through a total of 116 ×116 frequency-bin combinations for coincidence measurements ($k \in \{\pm 1, \ldots, \pm 117\}$) (Fig. 2); the $k = \pm 1$ bin pair is clipped by the DWDMs. The ~10 closest pairs experience higher accidental coincidences from residual pump light, which would necessitate additional DWDMs for further noise suppression. As examples, the measured coincidence-to-accidental ratios (CARs) for TE (TM) inputs increase from 1.3 (1.8) at $k = \pm 2$ to 33 (43) at $k = \pm 11$, and finally reach 260 (360) at $k = \pm 117$. From heuristic fitting based on coincidence and single-detector count rates [20], we estimate on-chip pair generation rates of

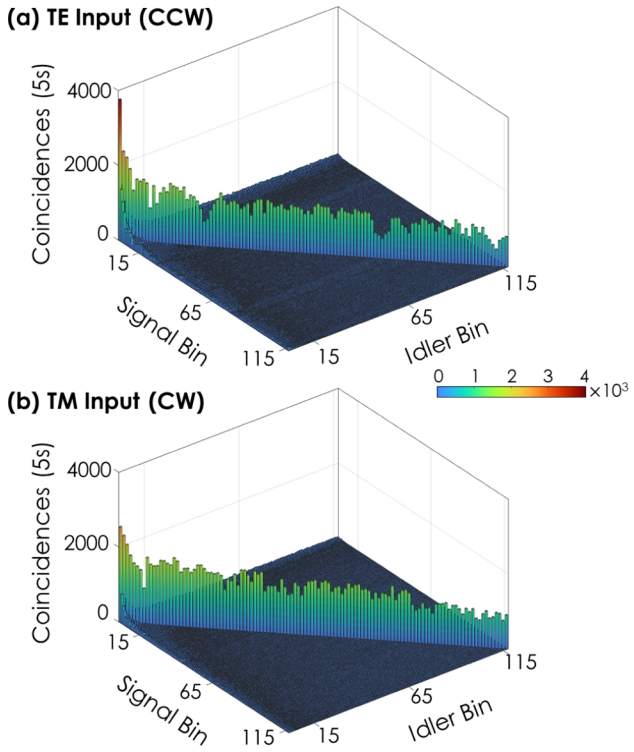

Fig. 2. Unidirectionally pumped JSIs measured for bins $k \in \{2, \ldots, 117\}$ with a 1-ns coincidence window. (a) TE-polarized input for counterclockwise (CCW) pumping only. (b) TM-polarized input for clockwise (CW) pumping only. Strong correlations are observed in energy-matched resonances, while other combinations exhibit levels close to accidental coincidences. Excessive noise in the first 10 bin pairs is attributed to residual pump light.

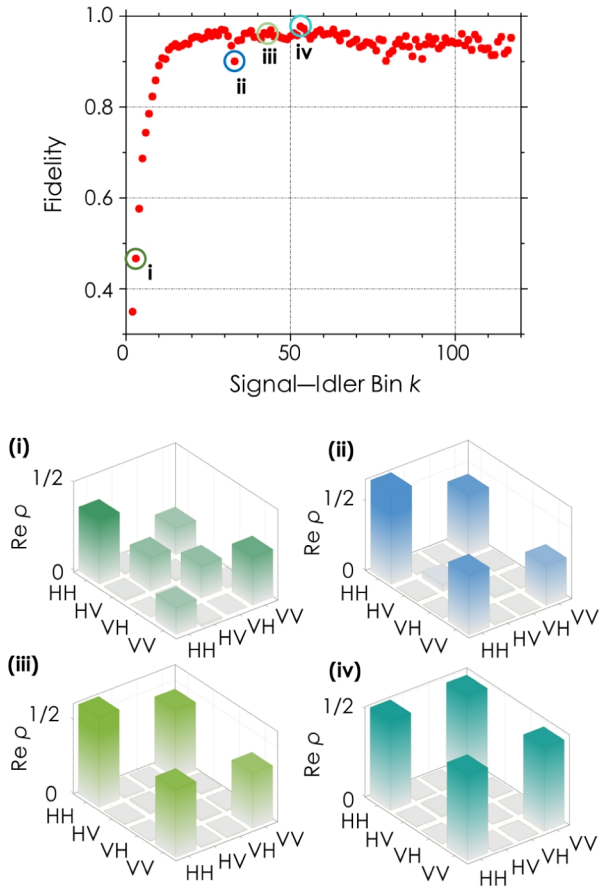

Fig. 3. Bayesian-estimated fidelities with respect to $|\Phi^+\rangle$ for 116 energy-matched frequency bins, along with corresponding density matrices (real part) for select bins (i)–(iv). The magnitudes of all imaginary components are less than 0.01 and are omitted for clarity.

~10^7 s^{-1} per bin, comparable to previous values reported in silicon as highlighted, e.g., by tables summarizing the literature on integrated photon sources [21,22]. No significant decrease in coincidence counts—relative to the fluctuations across the spectrum—was observed within the 9 THz examined, consistent with theoretical modeling [23] predicting a 3-dB SFWM bandwidth of ~20 THz: a bandwidth far beyond the C+L-band coverage of our measurement system that would require S-band (1460–1530 nm) and U-band (1625–1675 nm) components for a more thorough analysis.

We conduct polarization QST on these 116 energy-matched bin pairs after adjusting the pump polarization to balance output amplitudes from the two counterpropagating processes. We scan through 36 polarization projections, collecting coincidence counts (30 s per projection) for subsequent Bayesian state analysis [24–26]. For each bin pair, we infer 1024 density matrix samples from the gathered dataset and apply local rotations numerically to align the measured reference frame with that of the chip [27], enabling the calculation of quantum state fidelity and other entanglement metrics. Fidelities with respect to $|\Phi^+\rangle$ are depicted in Fig. 3. As expected, fidelities are lower for channels closer to the pump frequency [cf. density matrix (i)], but steadily improve with increasing channel separation, reaching a plateau within the range of approximately 90–98% across the rest of the spectrum. Four example density matrices (i)–(iv) are shown in Fig. 3 for a noisy bin near the pump resonance and bins at the minimum, average, and maximum fidelity, over the range $k \in [\![1, 117]\!]$. The cause of the fluctuations in this region is attributed to polarization or coupling drifts during the full measurement procedure which could be rectified with a polarization feedback loop or affixing the fiber array to the die. The average fidelity for all bins is 92(9)%, increasing to 94(2)% when excluding $k \in [\![2, 10]\!]$. These results mark a record number of fully characterized polarization-entangled channels from an integrated source, paving the way for ultracompact CMOS sources for quantum networking. The high fidelity, coupled with the corresponding average purity ($P = \mathrm{Tr}\rho^2$) of 0.92(2) for $k \in [\![1, 117]\!]$, indicates strong separability between the polarization and frequency degrees of freedom—a necessary but not sufficient condition for hyperentanglement. Valuable for quantum communication protocols such as dense coding [28] and entanglement distillation [29,30], hyperentanglement could be confirmed in future tests via measurements in the joint polarization-frequency domain [31].

Given the combination of narrow bin spacing and full C+L-band coverage, this source is well suited for dense multiplexing in the flex-grid paradigm of entanglement distribution, in which WSSs dynamically partition a broadband biphoton spectrum into numerous slots of energy-correlated bands and subsequently route them to multiple destination nodes (users) to establish entanglement links [2–4]. In the simplest scenario, assigning one frequency bin pair to each pair of users could support high-fidelity entanglement for more than 100 pairs of nodes

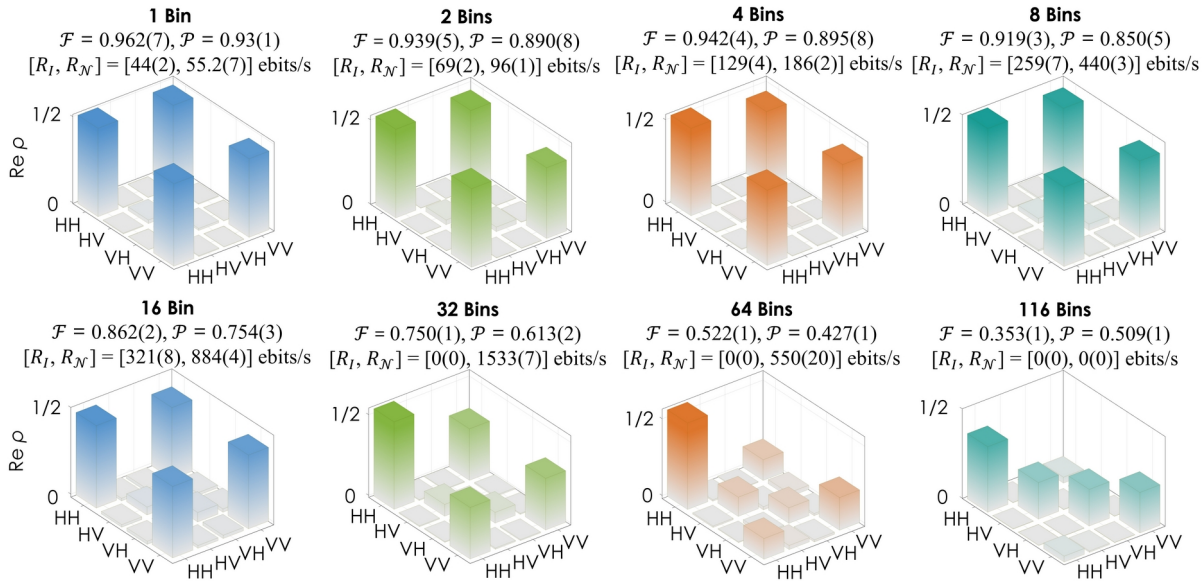

Fig. 4. Experimentally measured density matrices (real part) for $\{1, 2, 4, 8, 16, 32, 64, 116\}$ grouped frequency bins, their fidelity F with respect to $|\Phi^+\rangle$, purity P, and lower and upper bounds of distillable entanglement, all obtained from Bayesian QST. The imaginary components of all density matrices (not shown) are smaller than 0.03.

(cf. Fig. 3), constrained only by the WSS passband and number of output fibers. As certain users contend with increased link losses or seek additional services, we have the flexibility to group adjacent bins together for reallocation, effectively enhancing the coincidence rate. However, such bandwidth expansion can easily decrease fidelity: unless otherwise limited by background noise, increasing flux reduces CAR due to higher multipair-induced accidentals [20], and wider-bandwidth channels are more sensitive to any PMD present.

Consequently, achieving a delicate balance between optimizing throughput and maintaining entanglement quality above a predefined, application-specific threshold becomes a crucial area for investigation. Figure 4 offers an initial glimpse into this exploration, illustrating how bin grouping impacts state quality as evaluated through polarization QST. Our approach involves initially passing one bin on each side of the spectrum ($k = 58$) and symmetrically widening the filter passband, resulting in output states composed of $\{2, 4, 8, 16, \ldots\}$ contiguous frequency bins. As anticipated, fidelity decreases with larger bin groupings, while the coincidence rate rises—a trade-off which we can quantify through the entangled bit rate (EBR) defined as the distillable entanglement times the coincidence rate [27]. Lower and upper bounds on EBR (ebits/s), $[R_I, R_N]$, can be obtained from the coherent information [32] and log-negativity [33], respectively, as included in Fig. 4. In general, EBR increases as bins are grouped together due to the rising flux but eventually decreases as the polarization state becomes increasingly mixed. These findings highlight the flexibility of our compact design to accommodate end-user demands and varying channel conditions.

For insight into the nonidealities present in our system, we propose a model of a two-photon polarization state that incorporates accidental coincidences and imbalance and decoherence between $|HH\rangle$ and $|VV\rangle$ amplitudes. This theoretical density matrix is $\rho_T = \lambda\rho_{AB} + (1-\lambda)\rho_A \otimes \rho_B$, where ρ_{AB} is the density matrix of two time-correlated photons subject to decoherence and H/V imbalance, given by

$$\rho_{AB} = h|HH\rangle\langle HH| + g\sqrt{h(1-h)}|HH\rangle\langle VV| + g\sqrt{h(1-h)}|VV\rangle\langle HH| + (1-h)|VV\rangle\langle VV|. \quad (1)$$

Here $\lambda \in (0, 1]$ parameterizes multipair emission (ideally 1), $h \in [0,1]$ denotes the relative probability of $|HH\rangle$ compared to $|VV\rangle$ (ideally 0.5), and $g \in (0, 1]$ quantifies the quantum coherence (ideally 1)—without loss of generality assumed real and positive because of the local rotations performed to align the empirical density matrix with $|\Phi^+\rangle$ [27]. Given the starting bin at $k = 58$ (far from the pump), we assume accidentals are dominated by uncorrelated pairs rather than background; the accidentals contribute to the state in the form of a product of marginal density matrices $\rho_A = \mathrm{Tr}_B\,\rho_{AB} = h|H\rangle\langle H| + (1-h)|V\rangle\langle V| = \mathrm{Tr}_A\,\rho_{AB} = \rho_B$. The overlap of the model state with the ideal $|\Phi^+\rangle$ is $\mathsf{F}_T = \langle\Phi^+|\rho_T|\Phi^+\rangle = \frac{1}{2} - (1-\lambda)h(1-h) + g\lambda\sqrt{h(1-h)}$.

While simple, this model matches experimental observations well; numerical fits of $\rho_T(\lambda, h, g)$ to the experimentally determined density matrices in Fig. 4 agree with greater than 95% fidelity in all cases. Although the extracted H/V imbalance varies slightly ($h \in [0.52, 0.68]$), likely due to pump polarization drift during the full measurement, its impact on fidelity is negligible compared with that of accidentals: $\lambda = 0.95$ at 1 bin but by 32 bins has dropped sufficiently ($\lambda = 0.71$) to reduce R_I to zero. Incidentally, R_N is still large, highlighting the comparatively wide spread in these lower and upper bounds. Overall, this scaling emphasizes and quantifies the inherent fidelity-flux trade-off for these sources [4,20], from which a desired operating point can be chosen for a specific application.

On the coherence front, $g > 0.92$ until the 64- and 116-bin cases, where $g = 0.59$ and $g = 0.39$, respectively. With polarization-dependent delay in the WSS rated at < 0.5 ps (and measured at ~ 0.1 ps with a PMD tester), it is unsurprising to see such a reduction in coherence for broad bandwidths of several THz; quantitative predictions would require further tests to determine the orientation of the PMD principal axes with respect to the state's H/V modes [34].

However, it is important to note that although sensitive to off-chip PMD, our design is automatically robust to small path length mismatch on the chip itself. To see this, consider the theoretical quantum state, including both polarization and spectral degrees of freedom, subject to some additional delay τ on the VV component: $|\Psi\rangle \propto \iint d\omega_A d\omega_B\, \phi(\omega_A, \omega_B) \left(|HH\rangle + e^{i(\omega_A+\omega_B)\tau}|VV\rangle\right)$, where $\phi(\omega_A, \omega_B)$ is the joint spectral amplitude. For a monochromatic pump at ω_0, the spectrum can be expressed as $\phi(\omega_A, \omega_B) = \tilde{\phi}(\omega_A)\delta(\omega_A + \omega_B - 2\omega_0)$, and thus $|\Psi\rangle \propto \int d\omega_A\, \tilde{\phi}(\omega_A)\left(|HH\rangle + e^{2i\omega_0\tau}|VV\rangle\right)$. That is, the polarization component's phase depends only on the pump frequency and is maximally entangled irrespective of τ. In the context of a realistic pump with finite linewidth, the same reasoning holds as long as τ is much less than the laser coherence time, which in our case is ~5 μs, corresponding to a path mismatch of hundreds of meters in a 500 nm×220 nm silicon waveguide. Such PMD cancellation is a fascinating feature of entangled photon pairs [34,35] and an additional source of robustness in our source design; despite not being a "Sagnac" in the sense of truly common paths, insensitivity to small path variations is still obtained.

In summary, we propose and test a novel, compact, CMOS-fabricated photonic integrated circuit for the generation of high-fidelity polarization-entangled photons over a broad band. Our design has potential application for quantum networking as an entangled source and can tune the EBR through flex-grid networking.

Funding. U.S. Department of Energy, Office of Science; Advanced Scientific Computing Research (ERKJ353, DE-SC0024257); National Science Foundation (1747426-DMR, 2034019-ECCS); Air Force Research Laboratory (FA8750-20-P-1705).

Acknowledgments. Preliminary results were presented at IEEE IPC 2023 as paper number PD5. A portion of this work was performed at Oak Ridge National Laboratory, operated by UT-Battelle for the U.S. Department of Energy under contract no. DE-AC05-00OR22725.

Disclosures. The authors declare no conflicts of interest.

Data availability. Data available from the authors on request.

REFERENCES

1. S. Wehner, D. Elkouss, and R. Hanson, "Quantum internet: a vision for the road ahead," Science **362**, eaam9288 (2018).
2. N. B. Lingaraju, H.-H. Lu, S. Seshadri, *et al.*, "Adaptive bandwidth management for entanglement distribution in quantum networks," Optica **8**, 329–332 (2021).
3. F. Appas, F. Baboux, M. I. Amanti, *et al.*, "Flexible entanglement-distribution network with an AlGaAs chip for secure communications," npj Quantum Inf. **7**, 118 (2021).
4. M. Alshowkan, B. P. Williams, P. G. Evans, *et al.*, "Reconfigurable quantum local area network over deployed fiber," PRX Quantum **2**, 040304 (2021).
5. O. Gerstel, M. Jinno, A. Lord, *et al.*, "Elastic optical networking: a new dawn for the optical layer?" IEEE Commun. Mag. **50**, s12–s20 (2012).
6. N. Matsuda, H. Le Jeannic, H. Fukuda, *et al.*, "A monolithically integrated polarization entangled photon pair source on a silicon chip," Sci. Rep. **2**, 817 (2012).
7. L. Olislager, J. Safioui, S. Clemmen, *et al.*, "Silicon-on-insulator integrated source of polarization-entangled photons," Opt. Lett. **38**, 1960–1962 (2013).
8. L.-T. Feng, M. Zhang, Z.-Y. Zhou, *et al.*, "Generation of a frequency-degenerate four-photon entangled state using a silicon nanowire," npj Quantum Inf. **5**, 90 (2019).
9. F. Baboux, G. Moody, and S. Ducci, "Nonlinear integrated quantum photonics with AlGaAs," Optica **10**, 917 (2023).
10. G. Moody, L. Chang, T. J. Steiner, *et al.*, "Chip-scale nonlinear photonics for quantum light generation," AVS Quantum Sci. **2**, 041702 (2020).
11. M. Kues, C. Reimer, J. M. Lukens, *et al.*, "Quantum optical microcombs," Nat. Photonics **13**, 170–179 (2019).
12. H.-H. Lu, M. Liscidini, A. L. Gaeta, *et al.*, "Frequency-bin photonic quantum information," Optica **10**, 1655–1671 (2023).
13. Q. Zhang, K. Wu, and A. W. Poon, "Polarization entanglement generation in silicon nitride waveguide-coupled dual microring resonators," Opt. Express **32**, 22804–22816 (2024).
14. J. Suo, S. Dong, W. Zhang, *et al.*, "Generation of hyper-entanglement on polarization and energy-time based on a silicon micro-ring cavity," Opt. Express **23**, 3985–3995 (2015).
15. W. Wen, W. Yan, C. Lu, *et al.*, "Polarization-entangled quantum frequency comb from a silicon nitride microring resonator," Phys. Rev. Appl. **20**, 064032 (2023).
16. N. M. Fahrenkopf, C. McDonough, G. L. Leake, *et al.*, "The AIM Photonics MPW: a highly accessible cutting edge technology for rapid prototyping of photonic integrated circuits," IEEE J. Sel. Top. Quantum Electron. **25**, 1–6 (2019).
17. D. Dai, L. Liu, S. Gao, *et al.*, "Polarization management for silicon photonic integrated circuits," Laser Photonics Rev. **7**, 303–328 (2013).
18. AIM Photonics, "Analog Photonics - SUNY Poly Component Library," https://www.aimphotonics.com/apsuny-component-library (2024).
19. L. M. Cohen, S. Fatema, V. V. Wankhade, *et al.*, "Fine-resolution silicon photonic wavelength-selective switch using hybrid multi-mode racetrack resonators," J. Lightwave Technol. **42**, 4503–4510 (2024).
20. J. Alnas, M. Alshowkan, N. S. V. Rao, *et al.*, "Optimal resource allocation for flexible-grid entanglement distribution networks," Opt. Express **30**, 24375–24393 (2022).
21. C. Ma, X. Wang, V. Anant, *et al.*, "Silicon photonic entangled photon-pair and heralded single photon generation with CAR >12,000 and $g^{(2)}(0) < 0.006$," Opt. Express **25**, 32995–33006 (2017).
22. T. J. Steiner, J. E. Castro, L. Chang, *et al.*, "Ultrabright entangled-photon-pair generation from an AlGaAs-on-insulator microring resonator," PRX Quantum **2**, 010337 (2021).
23. Y. K. Chembo, "Quantum dynamics of Kerr optical frequency combs below and above threshold: Spontaneous four-wave mixing, entanglement, and squeezed states of light," Phys. Rev. A **93**, 033820 (2016).
24. R. Blume-Kohout, "Optimal, reliable estimation of quantum states," New J. Phys. **12**, 043034 (2010).
25. J. M. Lukens, K. J. H. Law, A. Jasra, *et al.*, "A practical and efficient approach for Bayesian quantum state estimation," New J. Phys. **22**, 063038 (2020).
26. H.-H. Lu, K. V. Myilswamy, R. S. Bennink, *et al.*, "Bayesian tomography of high-dimensional on-chip biphoton frequency combs with randomized measurements," Nat. Commun. **13**, 4338 (2022).
27. M. Alshowkan, J. M. Lukens, H.-H. Lu, *et al.*, "Broadband polarization-entangled source for C +L-band flex-grid quantum networks," Opt. Lett. **47**, 6480–6483 (2022).
28. J. T. Barreiro, T.-C. Wei, and P. G. Kwiat, "Beating the channel capacity limit for linear photonic superdense coding," Nat. Phys. **4**, 282–286 (2008).
29. C. Simon and J.-W. Pan, "Polarization entanglement purification using spatial entanglement," Phys. Rev. Lett. **89**, 257901 (2002).
30. Y.-B. Sheng and F.-G. Deng, "Deterministic entanglement purification and complete nonlocal Bell-state analysis with hyperentanglement," Phys. Rev. A **81**, 032307 (2010).
31. H.-H. Lu, M. Alshowkan, K. V. Myilswamy, *et al.*, "Generation and characterization of ultrabroadband polarization–frequency hyper-entangled photons," Opt. Lett. **48**, 6031–6034 (2023).
32. B. Schumacher and M. A. Nielsen, "Quantum data processing and error correction," Phys. Rev. A **54**, 2629–2635 (1996).
33. G. Vidal and R. F. Werner, "Computable measure of entanglement," Phys. Rev. A **65**, 032314 (2002).
34. C. Antonelli, M. Shtaif, and M. Brodsky, "Sudden death of entanglement induced by polarization mode dispersion," Phys. Rev. Lett. **106**, 080404 (2011).

35. M. Shtaif, C. Antonelli, and M. Brodsky, "Nonlocal compensation of polarization mode dispersion in the transmission of polarization entangled photons," Opt. Express **19**, 1728–1733 (2011).